ISPRS Annals of the Photogrammetry, Remote Sensing and Spatial Information Sciences, Volume XI-1-2026
XXV ISPRS Congress 2026 “From Imagery to Understanding”, Commission I, 4–11 July 2026, Toronto, Canada

Motion Correction for Scanning of Moving Objects using LiDAR: Experimental Validation and Analysis

Salil Goel* and Abhishek Yadav

Geoinformatics Laboratory, Department of Civil Engineering, IIT Kanpur, Kanpur, Uttar Pradesh, India
Email: sgoel@iitk.ac.in, abhishek.iitk.gi@gmail.com

Keywords: Motion Correction, LiDAR, Moving Objects, Terrestrial Laser Scanner, Error Analysis

Abstract

Conventional laser scanning techniques (such as in a Terrestrial Laser Scanner or Mobile mapping), whether used in a static or mobile mode require the object of interest to remain stationary during the scanning stage. Any motion of the object during scanning results in the apparent distortions in the resulting point cloud. The authors in (Goel and Lohani, 2014b) proposed a motion correction technique to estimate the 3D geometry of a moving object, utilizing a fusion of inertial and GNSS (Global Navigation Satellite Systems) sensors and transformation of the resulting point cloud to an object body coordinate system (OBCS). This paper aims to carry out the experimental validation and performance analysis of the motion correction method. Field experiments are designed and conducted in three phases to verify the correctness of the method. Through this, the paper aims to uncover insights into the performance of the motion correction algorithm and provide the first experimental validation of the proposed technique.

1. Introduction

The advancement of LiDAR (Light Detection and Ranging) technology has revolutionized the creation of precise and intricate 3D models by capturing dense point clouds. Static 3D laser scanners excel at acquiring detailed spatial data from objects of varying complexities. The introduction of laser scanners in conjunction with navigation sensors such as the Global Navigation Satellite System (GNSS) and Inertial Measurement Unit (IMU) has enabled the acquisition of highly accurate point clouds in a kinematic mode, allowing unrestricted movement of the laser scanner (Puente et al., 2011, Poppl et al., 2024, Guan et al., 2016). This integration has been used on aircraft to develop airborne mapping systems and on ground-based vehicles for terrestrial mobile mapping systems (Ilci and Toth, 2020, Stefano et al., 2021, Elhashash et al., 2022). Terrestrial laser scanning has been used extensively to generate detailed 3D models of urban environments (Li et al., 2017), forests (D’hont et al., 2024), as well as in construction sector (Aryan et al., 2021). However, all these techniques, whether static or mobile, rely on the fundamental assumption that the object being scanned remains stationary throughout the scanning process, devoid of any temporal movement (Goel and Lohani, 2014b). The inherent challenge arises when the object of interest is in motion, rendering it impossible to generate an accurate representation of its true shape through existing techniques. This limitation emerges due to the dynamic nature of moving objects, causing individual points on the surface to possess varying instantaneous coordinates during scanning. Consequently, the resulting point cloud lacks the essential shape information of the object, rendering it incorrect (Goel and Lohani, 2014b). This issue presents practical complications in numerous scenarios, such as scanning a ship docked in a harbor, capturing a hot air balloon whether untethered or tethered in place, or documenting the movements of a large crane, among others (Goel and Lohani, 2014b).

The authors in (Goel and Lohani, 2014b) proposed a *motion correction algorithm* to correct the distortions introduced due to the motion of the object and estimate the *true* geometry of the moving object. This algorithm operates under the assumption that the position and orientation data of the moving object can be acquired remotely through tracking devices, positioning and attitude sensors, or alternative methods. The key aspect of this method revolves around the conversion of laser scanner data, typically presented in a local coordinate system, into a new reference frame known as the Object Body Coordinate System (OBCS). The OBCS is fixed to the object body, regardless of the motion of the object. The transformation from a Global Coordinate System to OBCS and the positional vector of any point on the object (car) is shown in figure 1.

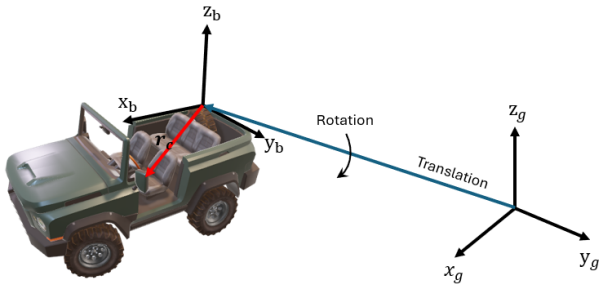

Figure 1. Relationship between a Global coordinate system (denoted by ’g’) and OBCS (denoted by ’b’). The position vector of a point on the car in OBCS is denoted by the vector r_c (shown in red).

Although other methods for scanning moving objects have been proposed (such as (Blais et al., 2004, Weise et al., 2007)), motion correction method is the only method that does not depend on the scanning pattern utilized, the distance of object from the laser scanner or the size of the object to be scanned, and makes no assumption about any of these. The motion correction equation demonstrating the transformation of a point on the object from a global coordinate system to OBCS is given by equation 1. The position of a point on the object in the global

* Corresponding author

This contribution has been peer-reviewed. The double-blind peer-review was conducted on the basis of the full paper.
https://doi.org/10.5194/isprs-annals-XI-1-2026-201-2026 | © Author(s) 2026. CC BY 4.0 License.

coordinate system (G) is denoted by r_t^G, with subscript t denoting the time-varying nature of the coordinate vector due to the motion of the object. The origin of OBCS in G is denoted by P_t^G, ${}_E R_t^B$ denotes the rotation matrix from Earth Tangential (denoted by E) coordinate system to OBCS (denoted by B) and ${}_G R_t^E$ denotes the rotation matrix from G to E at any time t. One of the simplest ways to observe the motion of the object is to make use of an integrated GNSS and INS (Inertial Navigation System) system, installed rigidly on the moving object. In this case, P_t^G denotes the location of the GNSS/INS system installed on the moving object. Interestingly, the authors in (Goel and Lohani, 2014b) demonstrated that the proposed motion correction equation is unaffected by any errors in the lever arm vector between GNSS and inertial sensors.

$$r^B = {}_E R_t^B \, {}_G R_t^E (r_t^G - P_t^G) \tag{1}$$

The motion-corrected coordinates are obtained in B frame and is denoted by r^B in equation 1. Although the authors in (Goel and Lohani, 2014a) presented the complete error model for the motion correction method, no experimental validation or performance analysis in the real-world is demonstrated. Therefore, this paper presents the real-world performance analysis of the motion correction method, and aims to validate the theoretical error model developed by (Goel and Lohani, 2014a) with the real-world observations. The remaining paper is divided into 4 sections. Section 2 presents the complete experimental setup established for validation and performance analysis of motion correction method. The results, analysis and a comparison with the theoretical models developed by (Goel and Lohani, 2014a) is presented in section 3. The conclusions of the paper and some avenues for future work are discussed in section 4.

2. Methodology and Experimental Setup

The data collection is done in an open environment, where GNSS signals are available. An integrated GNSS/INS system (Xsens MTi-680G (Xsens, 2025)) is installed on a moving object (a car) as shown in figure 2. An additional GNSS receiver (Trimble R10 (Trimble, 2025)) is also installed along with the Xsens system as a redundant system to detect potential errors in GNSS observations. The Xsens MTi-680G (Xsens, 2025) is used to estimate the motion of the car, i.e. derive its 6 DoF (Degrees of Freedom) including its 3D position and orientation in space. The moving car is scanned using REIGL VZ-2000i TLS (REIGL, 2025), installed on a tripod at a fixed point as shown in figure 3. The GNSS/INS data is logged on a laptop, kept inside the car, while the TLS data is logged on the onboard TLS storage. The motion correction algorithm requires all the sensors (including GNSS, Inertial sensors and TLS) to be precisely time synchronized. The synchronization between GNSS and Inertial sensors is easy, since they are physically colocated. However, the precise synchronization between GNSS and TLS is challenging due to the two sensors being physically apart. Hence, due to the unavailability of a reliable synchronization mechanism between GNSS and TLS, the experiments are conducted in a stop-and-go manner, wherein the car is moved to different locations, and then scanned while it is stationary. This is repeated multiple times and hence, the car ‘appears’ multiple times within the same dataset (refer section 3).

In addition to the sensors being synchronized, the motion correction algorithm also requires the trajectory, as well as the TLS dataset to be in the same coordinate reference frame. Since the trajectory solution from GNSS/INS is available in a global

Figure 2. Xsens Mti-680G and Trimble R10 installed on top of the moving car, on a tribrach. The INS of Xsens system is marked with a red square.

Figure 3. REIGL VZ-2000i TLS used for validation of motion correction algorithm, with the moving object (car) seen in the background.

coordinate system (specifically WGS-84 UTM 44N), the TLS data is also required to be transformed into the same reference system. Transformation of TLS from a local coordinate system associated with TLS to a global coordinate system is carried out using a standard georeferencing practice that involves the setting of ground control points (GCPs) using GNSS, which are then scanned using the TLS. To setup the GCPs, Trimble R10 GNSS receiver is installed at each of the GCPs and static GNSS observations are collected at each of the points for at least 30 minutes. The baseline processing of the GNSS observations (with base station installed at about 1.5 km) is carried out using Trimble Business Center (TBC) software (Center, 2025). Four such GCPs are setup in the test site, and circular target plates are installed at these GCPs. The heights of the target plates are measured using measuring tapes, and are then scanned using a TLS to establish a transformation from a local to global reference frame. Figure 4 shows a R10 GNSS receiver being used to setup GCPs and figure 5 shows a circular target plate installed at one of these GCPs. The key specifications of Xsens MTi-680G and REIGL VZ-2000i TLS are given in table 1 and table 2, respectively. A high-level flowchart depicting the role of multiple sensors and the motion correction algorithm to yield the motion corrected coordinates is shown in figure 6.

This contribution has been peer-reviewed. The double-blind peer-review was conducted on the basis of the full paper.
https://doi.org/10.5194/isprs-annals-XI-1-2026-201-2026 | © Author(s) 2026. CC BY 4.0 License.

Figure 4. GCPs are setup using Trimble R10 GNSS receiver. GNSS observation is recorded for at least 30 minutes at each GCP.

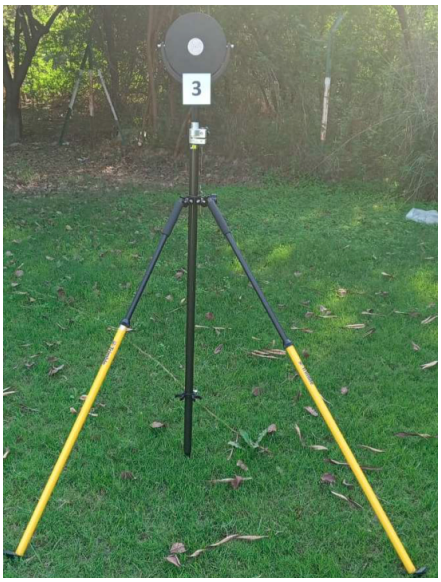

Figure 5. A circular target plate is installed at each of the GCPs. The identification of each GCP is mentioned alongside the target

Parameter	Value
Weight	98 grams
Dimensions	56.50 x 40.90 x 36.75 mm
Operating temperature	-40^oC to 80^oC
Roll & Pitch accuracy	0.2 deg RMS
Yaw accuracy	0.5 deg RMS
Update rate	upto 400 Hz
GPS	Single Frequency
Mounting orientation	No restriction
Casing material	Aluminum

Table 1. Key specifications of Xsens MTi 680G (Xsens, 2025).

The Xsens MTi-680G GNSS/INS is installed rigidly on top of the car using a tribrach (as seen in figure 2). Due to the metallic nature of materials used in the car, local magnetic distortions are observed in the magnetometer inside Xsens MTi-680G which affected the estimated attitudes. To account for such dis-

Parameter	Value
Weight	9.8 Kg
Dimensions	206 mm x 346 mm (dia x length)
Operating temperature	$0^o - +40^o$C
Wavelength	1550 nm
Maximum range	upto 2500 m
Field of View	100^o vertical x 360^o horizontal
Beam divergence	0.27 mrad
Pulse Repetition rate	upto 1.2 MHz
Accuracy	5 mm

Table 2. Key specifications of REIGL VZ-2000i TLS (REIGL, 2025).

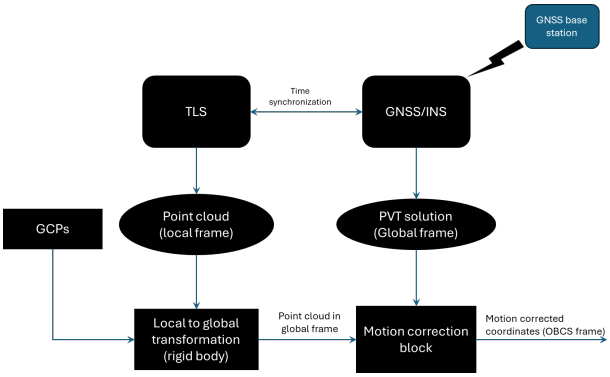

Figure 6. High level block diagram showing the processing of data from multiple sensors to yield the motion corrected coordinates.

tortions, the MTi sensor is recalibrated using a magnetic field mapper software (Manager, 2025), available with MTi-680G. To calibrate the Xsens sensor, the sensor is installed on to the car and the car is driven in a circular path at a speed of less than 15 Km/h, for about 4-5 times. The magnetic field mapper then checks for the magnetic anomalies and applies the corrections to the magnetic observations, ensuring that the magnetic norm is equal to 1. If the magnetic corrections are found to be unsatisfactory, the calibration process is repeated again. A screenshot of the magnetic field mapper software, with magnetic calibration is shown in figure 7. To further improve the

Figure 7. Magnetic field mapper software for calibration of Xsens MTi-680G.

accuracy of the Xsens, manual gyro bias estimation (MGBE), within the Xsens software (Manager, 2025) is used to estimate the biases in the gyroscope. During this phase, the vehicle (and the sensor) is kept stationary for a few minutes, after turning on the sensor for at least 10 minutes. The gravitational accelera-

tion is used to determine the inertial sensor biases in roll and pitch axes, while magnetic observations are used to estimate the biases along the yaw direction. The complete estimation is done within the Xsens software (called MT Manager (Manager, 2025)) using an EKF (Extended Kalman Filter) framework.

The motion correction experiment, wherein the moving car (with GNSS/INS installed) is scanned using REIGL VZ-2000i TLS is repeated 3 times. As explained earlier, due to the issues with synchronization of TLS with GNSS/INS sensors, the experiment is conducted in a stop-and-go manner, wherein the car is moved to different locations and then scanned with TLS while being stationary. Five such scan positions of the car for each of the three experiments are conducted. The data collected from TLS and GNSS/INS is combined and processed using equation 1 to yield motion corrected coordinates, which are further analyzed for accuracy analysis. The next section presents the results of these experiments in detail and analyzes the performance of the motion correction algorithm.

3. Results and Discussion

Of the three experiments conducted, this paper first presents the results of the first experiment in detail and then presents the results of the remaining two experiments. As mentioned earlier, the car is scanned in five distinct locations using TLS and the point cloud is transformed into global coordinate system using the standard rigid body transformation, involving a rotation and translation. This is carried out using the GCPs, which are also scanned with the same TLS. A visualization of the experimental site, with three car positions (shown in yellow box) and four GCPs (shown in red box) is shown in figure 8. Note that the car appears in multiple positions because it is moving while being scanned in a stop-and-go manner. If the car had been scanned while it is moving continuously, then the points would be seen spread out through the entire trajectory of the car (Goel and Lohani, 2014a). At each of the five scan positions, the attitude of the car is estimated using Xsens MTi-680G. To estimate the precision of the attitude updates, the inertial observations are taken for 20 minutes. The average values of the orientation in NED (North East Down) frame and their associated standard deviations are shown in table 3. It is observed that the attitude

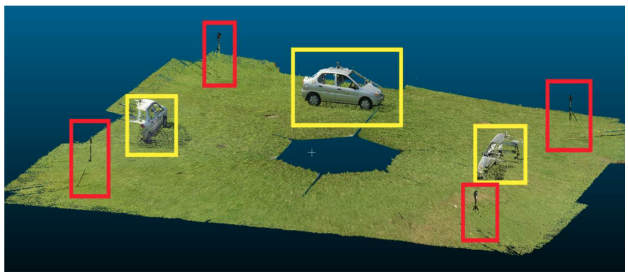

Figure 8. Visualization of the experimental setup with three different car locations (in yellow rectangles) and four GCPs (with circular targets; in red rectangles) are visible.

values obtained are within the prescribed specifications of the Xsens sensor. Since, the GNSS antenna provided with Xsens is a single frequency antenna, Trimble R10 installed along Xsens is used for obtaining the position of the car. As seen in figure 8, the car appears in multiple locations before application of the motion correction algorithm. After applying the motion correction algorithm, different scans of the car are expected to be

Scan	Roll (deg)		Pitch (deg)		Yaw (deg)	
	Value	SD	Value	SD	Value	SD
1	0.924	0.018	-1.482	0.029	172.210	0.122
2	1.446	0.024	-1.695	0.027	90.950	0.132
3	0.508	0.025	-1.359	0.033	10.707	0.072
4	1.069	0.038	-2.088	0.026	-85.848	0.0585
5	0.492	0.053	-1.618	0.044	144.437	0.486

Table 3. Attitude of the moving object at 5 different scan positions for the first experiment.

merged within a single scan, resulting in a cohesive and complete geometry of the car. The rotation matrix ${}_{E}R_{t}^{B}$ in equation 1 makes use of the attitude obtained from Xsens, while the rotation matrix ${}_{G}R_{t}^{E}$ includes the latitude and longitude of the origin of OBCS. An image of the point cloud of the car obtained, before applying the motion correction algorithm is shown in figure 9. Since, the car is scanned in a stop-and-go manner, the same car is visible in five different locations and orientations. After applying the motion correction algorithm, the different views of the car (i.e. motion corrected point cloud), where all five scans have merged are shown in figure 10 and figure 11.

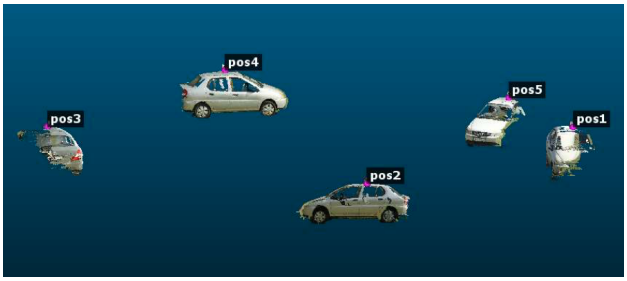

Figure 9. Point cloud of the car before applying the motion correction algorithm.

Figure 10. Side view of the car after applying the motion correction algorithm.

Visually, it can be seen that the motion correction algorithm is able to recreate the overall geometry of the car. Note that the motion correction algorithm does not make use of any point cloud registration techniques or point correspondences to regenerate the geometry. As stated earlier, the car appears in multiple places (as seen in figure 9) only because the experiment is conducted in a stop-and-go manner. If the experiment is conducted in a continuous manner, then the points would appear to spread across the entire trajectory of the vehicle (Goel and Lohani, 2014a), and extraction of any point correspondences would not be possible in such a case. For carrying out the quantitative error analysis, retro-reflective targets are installed

Figure 11. Top view (left) and front view (right) of the car after applying the motion correction algorithm.

at a few places on the body of the car, as shown in figure 12. The points $1-6$ marked on the car are used for estimation of errors due to the motion correction algorithm. Firstly, the re-

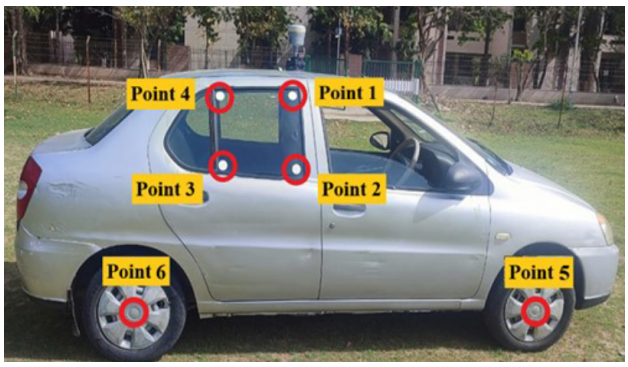

Figure 12. Retro-reflectors on the body of the car for quantitative error analysis of the motion correction algorithm.

flectance values of points $1-4$ are used to uniquely identify these points. These retro-reflectors can be easily identified in the scanned point cloud as seen in figure 13. Points $1-4$ are used to estimate the best fit plane for each of the five scan locations. Points $5-6$ are found by extracting the rim of wheel of the car, fitting a circle to the points and estimating the center of the circle. The segmented retro-reflectors $1-4$ are shown in figure 14. The segmented outer rim of tyre of the car is shown in figure 15 and the estimated best fit circle and the center of the circle (for targets $5-6$) is shown in figure 16. The relative orientation between the normals of the planes extracted from the five scans provides a quantitative estimate of the error due to the motion correction algorithm. Table 4 lists the angle between normals of the plane extracted from any two scans (of the five scan positions). The average rotational error between the normals of the planes is approximately 1.57^o. The highest rotational error observed is about 3.118^o between scans 3 and 4, while lowest error is about 0.38^o, observed between scans 2 and 5.

Further, the coordinates of all the six points are extracted in all the five scans and the resulting standard deviation of the points is plotted as a function of distance from origin of OBCS, which is the GNSS phase center in this case (Goel and Lohani, 2014b). This variation of standard deviation of the six points with distance from GNSS phase center is shown in figure 17. The au-

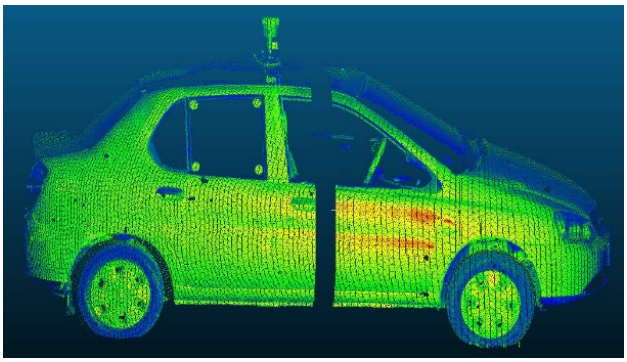

Figure 13. Retro-reflectors can be seen clearly in the LiDAR scans of the car.

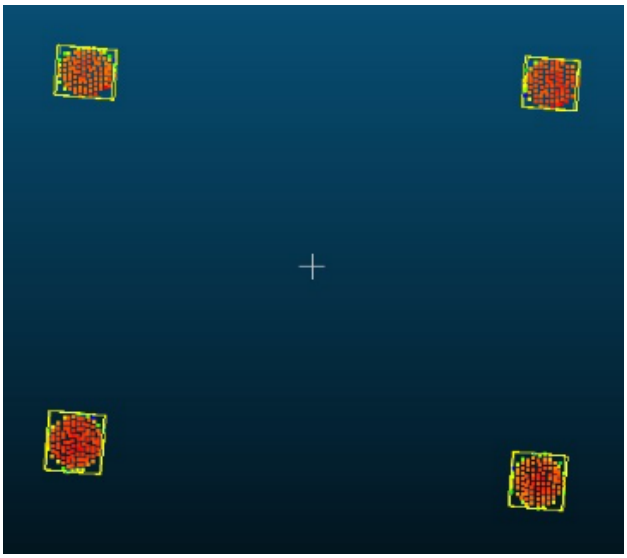

Figure 14. Extracted retro-reflectors $1-4$ from the car..

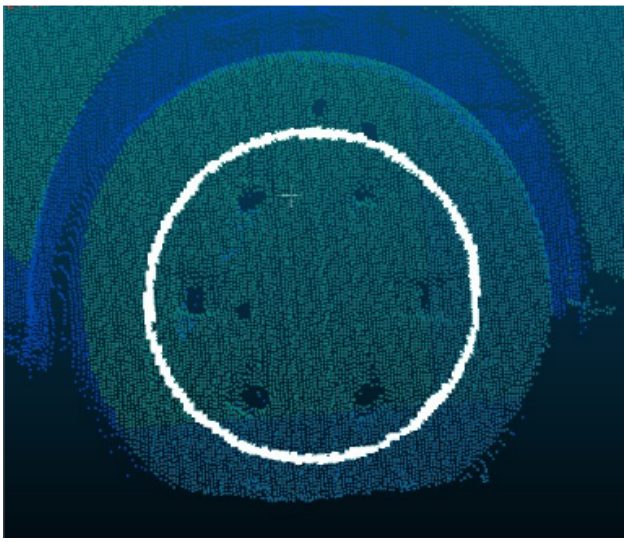

Figure 15. Segmented outer rim of tyre of the car containing the target 5 at the center.

thors in (Goel and Lohani, 2014a) modelled the errors due to the motion correction algorithm and hypothesized that the positional errors should increase with increasing distance from the

https://doi.org/10.5194/isprs-annals-XI-1-2026-201-2026 | © Author(s) 2026. CC BY 4.0 License.

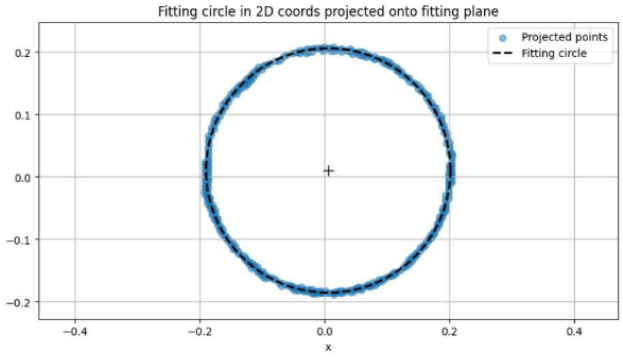

Figure 16. Estimated best fit circle and associated center to find the coordinates of target 5 in OBCS.

Scan Combination	Angle (in degrees)
1 and 2	1.315^o
1 and 3	1.326^o
1 and 4	1.807^o
1 and 5	1.053^o
2 and 3	0.764^o
2 and 4	2.890^o
2 and 5	0.38^o
3 and 4	3.118^o
3 and 5	0.498^o
4 and 5	2.758^o

Table 4. Angle between normals of the plane extracted in any two scans.

origin of OBCS (i.e. GNSS phase centre). The results shown in

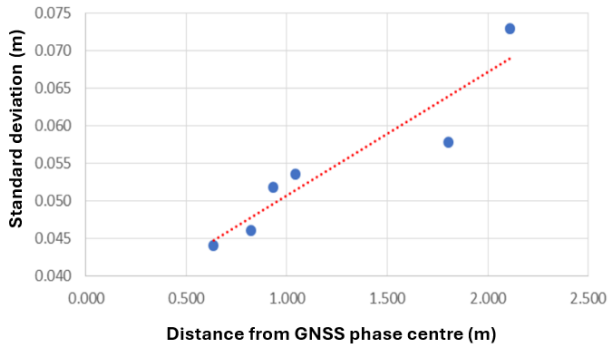

Figure 17. Variation of the standard deviation of the coordinates of the six points with distance from GNSS phase centre.

figure 17 provide an experimental validation of the error behaviour hypothesized by (Goel and Lohani, 2014a). Interestingly, it can be observed that the growth of errors is largely linear with increasing distance from GNSS phase centre. The motion correction error model proposed by (Goel and Lohani, 2014a) attributed errors to GNSS errors at short distances (from GNSS) and orientation errors from inertial sensors at larger distances from the GNSS. Furthermore, the authors estimated the positional errors to be in the order of 5 cm at for points within 10 m of the GNSS phase centre. Figure 17 shows that the standard deviation of the positional errors varies from about 4.5 cm to about 7 cm.

Following the error model proposed by (Goel and Lohani, 2014a), the theoretical error in the estimated coordinates of the points on the car is computed and is shown in figure 18. For the car, the errors are estimated to be larger around the tyres, front and back of the vehicle, minimum near the rooftop (where GNSS is installed). Although the estimated errors follow the same behaviour as modelled errors, the estimated errors are found to be larger in magnitude than the modelled errors. This is probably due to the effects of other systematic and/or random effects which remain unmodelled in the error model proposed by (Goel and Lohani, 2014a). The same experiment is repeated two more times to evaluate the repeatability of the observed patterns and the associated results are presented in figures 19 - 22. The mean rotational error between the planes formed by retro-reflectors $1-4$ for the second and third experiments is about 1.933^o and 1.684^o, respectively.

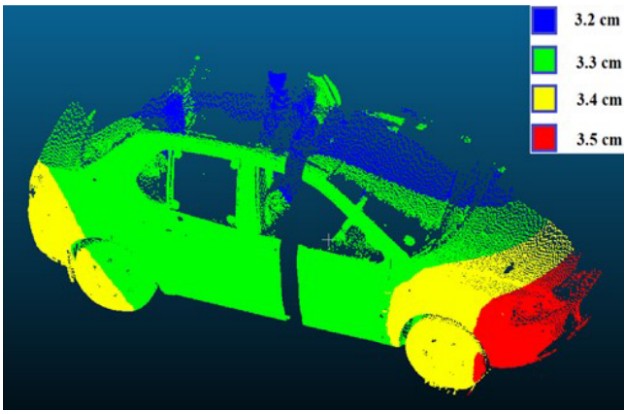

Figure 18. Modelled positional errors in the motion corrected point cloud obtained in OBCS.

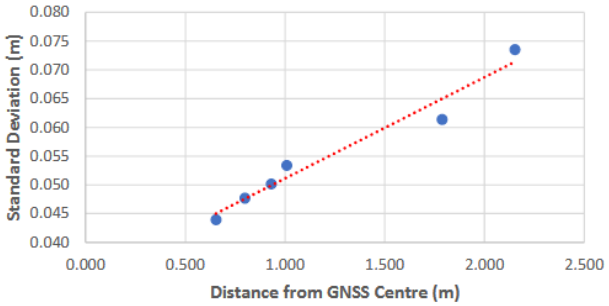

Figure 19. Variation of the standard deviation of the coordinates of the six points with distance from GNSS phase centre (for the second experiment).

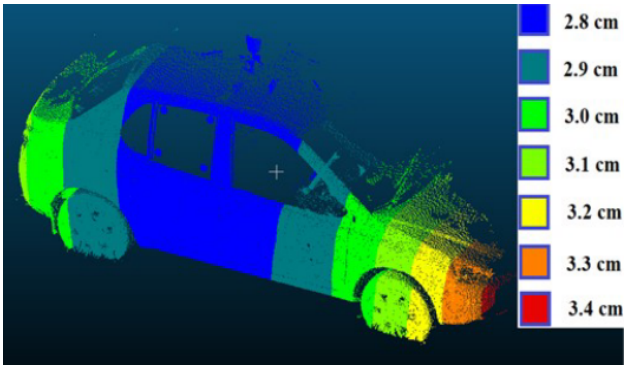

Figure 20. Modelled positional errors in the motion corrected point cloud obtained in OBCS (for the second experiment).

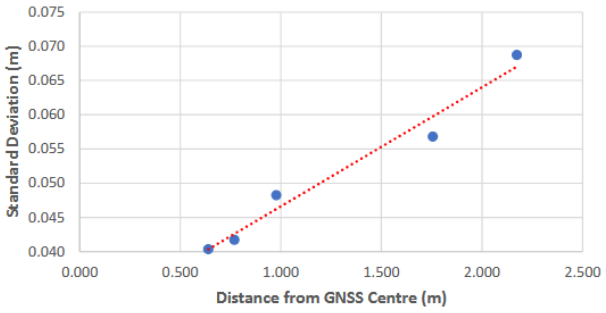

Figure 21. Variation of the standard deviation of the coordinates of the six points with distance from GNSS phase centre (for the third experiment).

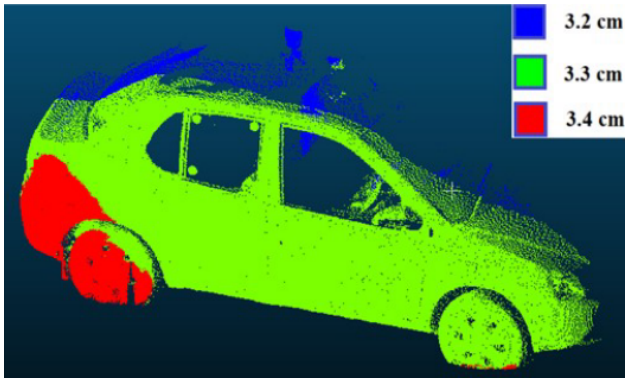

Figure 22. Modelled positional errors in the motion corrected point cloud obtained in OBCS (for the third experiment).

A plot of standard deviation in the targets for the second experiment is shown in figure 19 and the associated modelled errors for the same experiment is shown in figure 20. The results for the third experiment, including variation of the positional errors with distance from GNSS centre and modelled uncertainties is shown in figure 21 and figure 22, respectively. It can be observed from these figures that similar error behaviour is observed when the experiments are repeated multiple times. The positional errors increase linearly with increasing distance from GNSS centre and the estimated experimental positional uncertainties vary from about 4 cm to 8 cm, while modelled uncertainties vary from 3 cm to 4 cm. This discrepancy between modelled and estimated uncertainties can be attributed to simplified assumptions made by (Goel and Lohani, 2014a) in their error models, assumed optimistic performance of the sensors involved during the experiment and possibly due to some unmodelled effects. Despite the discrepancies in the magnitude of estimated and modelled uncertainties, the overall behaviour of the estimated uncertanties matches with the modelled uncertainties and thus, provides an experimental validation of the motion correction algorithm, and the associated error model. The next section presents the conclusions of the paper and discusses some ideas for the future work.

4. Conclusions and Future Work

This paper presented the experimental validation of the motion correction algorithm proposed by (Goel and Lohani, 2014b), that enabled 3D scanning of moving objects using LiDAR, allowing precise estimation of 3D geometry of such moving objects. The experimental validation and error analysis of the results is carried out using a car as a moving object, which is equipped with Xsens MTi-680G GNSS/INS and scanned with REIGL VZ-2000i TLS. The results demonstrate that the motion correction algorithm is able to successfully recreate the correct 3D geometry of the car. Furthermore, the results demonstrate that the error in the 3D position error varies from 4 cm to 7 cm, with GNSS errors being the largest contributor to the error budget. The experimentally derived errors were compared with the modelled errorrs estimated using the error budget proposed by (Goel and Lohani, 2014a). Although the magnitude of experimentally derived errors is larger as compared to modelled errors, the estimated errors follow the same general trend as observed from the error model of the motion correction algorithm. To the best of author’s understanding, this is the first experimental validation and error analysis of the motion correction algorithm.

Due to unavailability of a suitable time synchronization mechanism between TLS and other sensors, the experiments are conducted in a stop-and-go manner, thus simulating the movement of a car. The current evaluation does not account for errors due to sensor synchronization. Although the experimental evaluation is presented for a car as a moving object, the same is equally applicable to any other moving rigid object. In the future work, this paper will extend this work to a full-scale experimental evaluation incorporating the time synchronization among all sensors, thus accounting for errors due to time synchronization in the motion correction algorithm. Further, experimental validation and performance analysis of the motion correction algorithm when scanned using a mobile LiDAR will also be performed.

Acknowledgments

The authors would like to acknowledge the efforts of Saurabh Nishad, Shitla Tripathi, Ram Kewal Maurya, Vipul Sharma and Hari Babu Prajapati for assistance in data collection activities.

References

Aryan, A., Bosché, F., Tang, P., 2021. Planning for terrestrial laser scanning in construction: A review. *Automation in Construction*, 125, 103551. https://www.sciencedirect.com/science/article/pii/S0926580521000029.

Blais, F., Picard, M., Godin, G., 2004. Accurate 3d acquisition of freely moving objects. *Proceedings. 2nd International Symposium on 3D Data Processing, Visualization and Transmission, 2004. 3DPVT 2004.*, 422–429.

Center, T. B., 2025. Trimble Business Center Software. https://geospatial.trimble.com/en/products/software/trimble-business-center.

D’hont, B., Calders, K., Bartholomeus, H., Lau, A., Terryn, L., Verhelst, T., Verbeeck, H., 2024. Evaluating airborne, mobile and terrestrial laser scanning for urban tree inventories: A case study in Ghent, Belgium. *Urban Forestry Urban Greening*, 99, 128428. https://www.sciencedirect.com/science/article/pii/S1618866724002267.

Elhashash, M., Albanwan, H., Qin, R., 2022. A Review of Mobile Mapping Systems: From Sensors to Applications. *Sensors*, 22(11). https://www.mdpi.com/1424-8220/22/11/4262.

Goel, S., Lohani, B., 2014a. Error analysis of motion correction method for laser scanning of moving objects. *ISPRS Annals of the Photogrammetry, Remote Sensing and Spatial Information Sciences*, II-5, 139-144. https://isprs-annals.copernicus.org/articles/II-5/139/2014/.

Goel, S., Lohani, B., 2014b. A Motion Correction Technique for Laser Scanning of Moving Objects. *IEEE Geoscience and Remote Sensing Letters*, 11(1), 225-228.

Guan, H., Li, J., Cao, S., Yu, Y., 2016. Use of mobile LiDAR in road information inventory: a review. *International Journal of Image and Data Fusion*, 7(3), 219–242. https://doi.org/10.1080/19479832.2016.1188860.

Ilci, V., Toth, C., 2020. High Definition 3D Map Creation Using GNSS/IMU/LiDAR Sensor Integration to Support Autonomous Vehicle Navigation. *Sensors*, 20(3). https://www.mdpi.com/1424-8220/20/3/899.

Li, Z., Zhang, L., Mathiopoulos, P. T., Liu, F., Zhang, L., Li, S., Liu, H., 2017. A hierarchical methodology for urban facade parsing from TLS point clouds. *ISPRS Journal of Photogrammetry and Remote Sensing*, 123, 75-93. https://www.sciencedirect.com/science/article/pii/S0924271616305408.

Manager, M., 2025. Xsens MT Manager. https://www.xsens.com/hubfs/Downloads/usermanual/MT_Manager_user_manual.pdf.

Poppl, F., Ullrich, A., Mandlburger, G., Pfeifer, N., 2024. A flexible trajectory estimation methodology for kinematic laser scanning. *ISPRS Journal of Photogrammetry and Remote Sensing*, 215, 62-79. https://www.sciencedirect.com/science/article/pii/S0924271624002521.

Puente, I., González-Jorge, H., Arias, P., Armesto, J., 2011. LAND-BASED MOBILE LASER SCANNING SYSTEMS: A REVIEW. *The International Archives of the Photogrammetry, Remote Sensing and Spatial Information Sciences*, XXXVIII-5/W12, 163–168. https://isprs-archives.copernicus.org/articles/XXXVIII-5-W12/163/2011/.

REIGL, 2025. Specifications of REIGL VZ-2000i TLS. https://www.riegl.com/de-oesterreich/products/detail/RIEGL-vz-2000i.

Stefano, F. D., Chiappini, S., Gorreja, A., Balestra, M., Pierdicca, R., 2021. Mobile 3D scan LiDAR: a literature review. *Geomatics, Natural Hazards and Risk*, 12(1), 2387–2429. https://doi.org/10.1080/19475705.2021.1964617.

Trimble, 2025. Specifications of Trimble R10 GNSS. https://help.fieldsystems.trimble.com/r10/home.htm.

Weise, T., Leibe, B., Van Gool, L., 2007. Fast 3d scanning with automatic motion compensation. *2007 IEEE Conference on Computer Vision and Pattern Recognition*, 1–8.

Xsens, 2025. Specifications of Xsens MTi-680G. https://www.movella.com/sensor-modules/xsens-mti-680g-rtk-gnss-insspecifications.